

Critical Role of Ti^{4+} in Stabilizing High-Voltage Redox Reactions in Li-Rich Layered Material

Moses Cho, Seok Hyun Song, Seokjae Hong, Kyoung Sun Kim, Maxim Avdeev, Jong-Gyu Yoo, Kyung-Tae Ko, Jihyun Hong,* Jongsoon Kim,* Seongsu Lee,* and Hyungsub Kim*

Li-rich layered oxide materials are considered promising candidates for high-capacity cathodes for battery applications and improving the reversibility of the anionic redox reaction is the key to exploiting the full capacity of these materials. However, permanent structural change of the electrode occurring upon electrochemical cycling results in capacity and voltage decay. In view of these factors, Ti^{4+} -substituted Li_2IrO_3 ($Li_2Ir_{0.75}Ti_{0.25}O_3$) is synthesized, which undergoes an oxygen redox reaction with suppressed voltage decay, yielding improved electrochemical performance and good capacity retention. It is shown that the increased bond covalency upon Ti^{4+} substitution results in structural stability, tuning the phase stability from O3 to O1' upon delithiation during charging compared with O3 to T3 and O1 for pristine Li_2IrO_3 , thereby facilitating the oxidation of oxygen. This work unravels the role of Ti^{4+} in stabilizing the cathode framework, providing insight for a fundamental design approach for advanced Li-rich layered oxide battery materials.

for new cathodes with higher reversible capacities, numerous materials have attracted attention, including layered ($LiCoO_2$, $LiNi_xCo_yMn_{1-x-y}O_2$), spinel ($LiNi_{0.5}Mn_{1.5}O_4$), and olivine ($LiFePO_4$, $LiFe_xMn_{1-x}PO_4$) materials.^[2] Among these materials, Li-rich layered oxide materials have received significant attention because of their high energy density, with a particular focus on Li-rich $Li_{1.2}Ni_{0.13}Co_{0.13}Mn_{0.54}O_2$ (Li-rich NCM) materials.^[3] These materials composed of Ni, Co, and Mn can deliver a capacity of over 260 mAh g^{-1} , which is nearly two times that of conventional layered $LiCoO_2$ materials.^[4] Nevertheless, their application in EVs is restrained by their limited cycle life, structural degradation, and voltage fade issues, triggering significant research efforts to resolve these concerns.^[4a,5]

1. Introduction

Li-ion batteries (LIBs) are considered promising power sources for the recently growing electric vehicle (EV) market owing to their high gravimetric and volumetric energy densities. However, as existing LIBs do not yet meet the required energy density for EV applications, new efficient electrode materials with high energy density are needed.^[1] In the search

Coupled with identifying the descriptors affecting the electrochemical cycling, activating and stabilizing the anionic redox reaction during electrochemical cycling is a novel approach to realizing high capacity in Li-rich layered oxides, where the anionic redox is activated via oxygen oxidation in the high-voltage region. Recent studies have been conducted using the $Li_2Ir_{1-x}M_xO_3$ ($M = Sn$) system to better understand the origin of the oxygen redox reaction. McCalla et al. presented a

M. Cho, S. H. Song, S. Hong, K. S. Kim, Dr. S. Lee, Dr. H. Kim
Neutron Science Division
Korea Atomic Energy Research Institute (KAERI)
111 Daedeok-daero 989 Beon-Gil, Yuseong-gu, Daejeon 34 057, Republic of Korea
E-mail: seongsulee@kaeri.re.kr; hyungsubkim@kaeri.re.kr

S. H. Song, S. Hong, K. S. Kim
Department of Chemical and Biological Engineering
Korea University
145 Anam-Ro, Seongbuk-Gu, Seoul 0 2841, Republic of Korea

Dr. M. Avdeev
Australian Nuclear Science and Technology Organisation (ANSTO)
New Illawarra Rd, Lucas Heights, NSW 2232, Australia


J.-G. Yoo
Max Planck POSTECH/Hsinchu Center for Complex Phase Materials
67 Cheongam-ro, Pohang 37 673, Republic of Korea

J.-G. Yoo
Department of Physics
Pohang University of Science and Technology
67 Cheongam-ro, Pohang 37 673, Republic of Korea

Dr. K.-T. Ko
Research Center for Materials Analysis
Korea Basic Science Institute (KBSI)
169-148 Gwahak-ro, Yuseong-gu, Daejeon 34 133, Republic of Korea

Dr. J. Hong
Center for Energy Materials Research
Korea Institute of Science and Technology (KIST)
5 Hwarang-ro 14 Gil, Seongbuk-gu, Seoul 02792, Republic of Korea
E-mail: jihyunh@kist.re.kr

Prof. J. Kim
Department of Energy Science
Sungkyunkwan University
Suwon 16419, Republic of Korea
E-mail: jongsoonkim@skku.edu

 The ORCID identification number(s) for the author(s) of this article can be found under <https://doi.org/10.1002/sml.202100840>.

DOI: 10.1002/sml.202100840

visualization of the O–O peroxy-like structure through transmission electron microscopy (TEM) and neutron diffraction (ND) analyses.^[6] They further demonstrated that both the cationic and anionic redox occur simultaneously in the Li_2IrO_3 (LIO) system. Meanwhile, the recent work by Hong et al. has indicated that only Ir metal participates in the redox reaction of LIO, whereas the anionic redox becomes active upon Sn doping.^[7] This finding indicates that the distortion of the local structure by heteroatom doping triggers the oxygen redox via the formation of a strong O–O dimer between the Ir and migrated Sn, demonstrating the strong coupling between the oxygen redox and metal–oxygen decoordination. Thus, different mechanisms appear to exist at different local structures triggering different chemistry in the $\text{Li}_2\text{Ir}_{1-x}\text{M}_x\text{O}_3$ (M = metal ion) system.

One strategy to improve the electrochemistry and invoke intrinsic physiochemical properties is to introduce dopant elements into the system, with numerous studies on a wide range of doping elements conducted on layered oxide materials.^[8] Among such dopants, Ti^{4+} has shown interesting features, with the introduction of Ti^{4+} resulting in improved structural integrity, thereby stabilizing the structural and electrochemical performance stability in Li-based layered oxides,^[9] spinels,^[10] and Na-based layered materials.^[11] However, negative effects of Ti^{4+} substitution were also seen in $\text{Li}_2\text{Ru}_{1-x}\text{M}_x\text{O}_3$ (M = Mn, Sn, Ti), with voltage and capacity decay observed upon electrochemical cycling with Ti doping; the Ti ion migrated and was trapped in the tetrahedral site, hindering the Li shuttling path.^[12] Moreover, several studies have shown that Ti^{4+} doping activated oxygen oxidation, stabilizing the cyclability and facilitating the

anionic redox reaction in the high-voltage region.^[11a,c] Even though considerable research has been performed on the effect of Ti^{4+} doping in battery materials, an understanding of how Ti^{4+} ions can be integrated and regulate redox contributions between the metal and oxygen redox reactions remain lacking.

In this study, we reveal the critical role of Ti^{4+} in $\text{Li}_2\text{Ir}_{0.75}\text{Ti}_{0.25}\text{O}_3$ (LITO25) using a combination of X-ray diffraction (XRD), ND, and X-ray absorption microscopy (XAS) analyses and density functional theory (DFT) calculations. LITO25 exhibits a stabilized oxygen redox plateau in the high-voltage region, prompting a prolonged single-phase reaction with minimized phase transitions via improved structural stability upon Ti^{4+} substitution. Our findings provide insight into the potential role of dopants acting as both a stabilizer and enricher of the electrochemical performance for the design of cathode materials for future battery applications.

2. Results and Discussion

2.1. Structural Characterization of as-Synthesized $\text{Li}_2\text{Ir}_{1-x}\text{Ti}_x\text{O}_3$ ($x = 0, 0.25, 0.5, 0.75$)

$\text{Li}_2\text{Ir}_{1-x}\text{Ti}_x\text{O}_3$ ($x = 0, 0.25, 0.5, 0.75$) samples were prepared through solid-state synthesis, and the corresponding XRD patterns are presented in Figure 1a. The XRD peaks can be indexed to the monoclinic structure of $C2/m$ symmetry, where Li is partially substituted in the TM layer as LiM_2 sequence, forming an ordered honeycomb-like arrangement.^[6,13] There was no trace of impurity phases, indicating that samples were

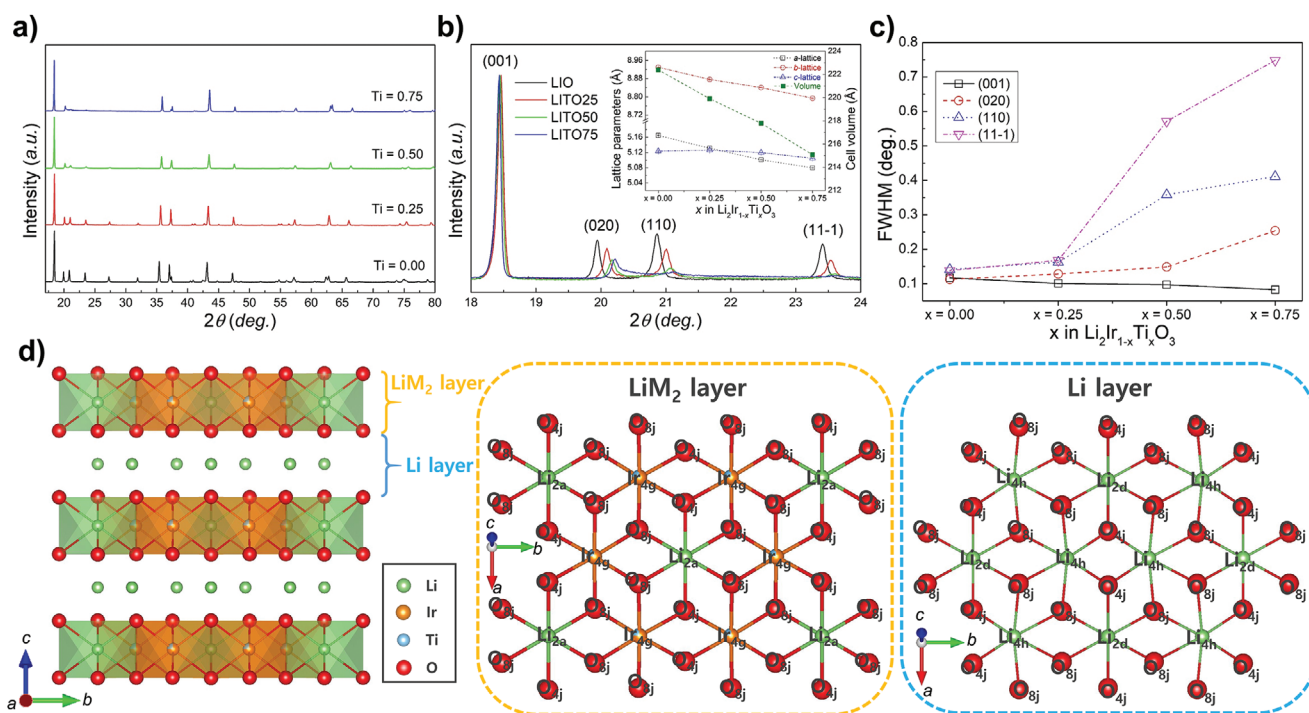


Figure 1. a) XRD patterns of $\text{Li}_2\text{Ir}_{1-x}\text{Ti}_x\text{O}_3$ ($x = 0, 0.25, 0.5, 0.75$). b) XRD patterns in 2θ range from 18° to 24° . Lattice parameter changes with different Ti^{4+} concentrations determined from profile fitting shown in the inset. c) FWHM data of XRD patterns of $\text{Li}_2\text{Ir}_{1-x}\text{Ti}_x\text{O}_3$ ($x = 0, 0.25, 0.5, 0.75$) on (001) and superstructure peaks. d) Structural representations of layered $\text{Li}_2\text{Ir}_{0.75}\text{Ti}_{0.25}\text{O}_3$ structure.

in the solid-solution state with Ti^{4+} thoroughly integrated into the LIO system. XRD patterns in the 2θ range of $18\text{--}24^\circ$ are presented in Figure 1b. With increasing Ti^{4+} content, the diffraction peaks shifted toward higher angle, which is attributed to Ti^{4+} having a smaller ionic radius (0.605 \AA) than Ir^{4+} (0.625 \AA). In addition, the lattice parameters and cell volume linearly decreased with increasing Ti^{4+} content, as shown in the inset of Figure 1b, which is a direct result of the smaller Ti^{4+} radii compared to Ir^{4+} .

Stacking faults were inherently present in the layered structures during synthesis due to the disordering of Li, Ir, and Ti ions in the LiM_2 layers, with corresponding XRD peaks, known as superstructure peaks, appearing between 19° and 23° .^{16,14} The degree of stacking faults can be deduced from the full width at half maximum (FWHM), as illustrated in Figure 1c, where a slight reduction of the FWHM of the main (001) peak and markedly increased superstructure peaks are observed. A decrease in the FWHM implies minimized stacking faults, whereas an increase in the FWHM indicates a high degree of stacking faults. With the addition of Ti^{4+} , a decrease in the XRD intensity of the superstructure peaks was observed while the crystallinity of the overall cathode frame was maintained. This finding suggests an increase of structural rearrangement through in-plane direction, indicating the effective role of stacking faults in tuning the local structures.

These results were further elaborated with the Rietveld refinement analysis of ND data for $\text{Li}_2\text{Ir}_{1-x}\text{Ti}_x\text{O}_3$ ($x = 0, 0.25, 0.5$) presented in Figures S1–S4 and Tables S1–S3, Supporting Information. The analysis revealed that Ti^{4+} was well integrated mainly at the Ir 4g site, with an increase of site mixing occurring within the LiM_2 layers as Ti^{4+} content increases, shown in Figure 1d. Ti^{4+} was also partially substituted at the Li 2a sites in the Li layer, and the effect of Ti^{4+} substitution was pronounced in the Li–O and Ir–O bonding distances, as summarized in Table S4, Supporting Information. Overall, the Li–O and Ir–O bond distances decreased linearly with increasing Ti^{4+} content in the LiM_2 layer, with the longest Li–O bond length decreasing in the order of 2.102, 2.073, and 2.062 \AA , and the long Ir–O bond contracting in the order of 2.04, 2.035, and 2.011 \AA for the LIO, LITO25, and LITO50 samples, respectively. This overall bond shrinkage can be explained by the strong Ti^{4+} –O ionic bond, as Ti^{4+} has the electronic configuration d^0 . The strong bonding ensures structural integrity, possibly stabilizing the oxygen redox reaction at high voltage while maintaining the structural rigidity. However, the Li–O bond in the Li layer underwent anisotropic bond length changes, with both shrinkage and elongation of lengths observed upon increasing the Ti^{4+} concentration. This result indicates the distortion of the LiO_6 octahedral, destabilizing the overall LiO_6 network in the Li layer, resulting in facilitated Li-ion transfer during electrochemical reaction, as will be discussed in later sections.

Selected area electron diffraction (SAED) and energy-dispersive X-ray spectroscopy (EDS) analyses of the TEM images (Figures S5 and S6, Supporting Information) were also performed to confirm the crystal structure and elemental distribution at the particle scale; the LITO25 sample was selected as a representative sample. The SAED pattern collected along the [001] zone axis revealed many reflections, with d-spacing analysis indexing them all as the $C2/m$ monoclinic structure.

Specifically, superstructure peaks were clearly observed in both (020) and (20-1), which agrees well with the XRD pattern. The TEM–EDS mapping of the LITO25 particle (Figure S6, Supporting Information) shows that the Ir, Ti, and O elements were well distributed in the particle, indicating that the synthesized material was in a single phase.

2.2. Galvanostatic Charge/Discharge Profiles of LIO and LITO25

The electrochemical performances of the $\text{Li}_2\text{Ir}_{1-x}\text{Ti}_x\text{O}_3$ ($x = 0, 0.25, 0.5, 0.75$) samples were evaluated in galvanostatic mode at a current rate of 20 mA g^{-1} in the voltage range of 2.5–4.6 V versus Li^+/Li . Voltage profiles for the first cycle at different Ti^{4+} concentrations are presented in Figure S7, Supporting Information. LIO exhibited a two-step voltage profile during the charge process and preserved it on the subsequent discharge, where the redox consisted of the Ir metal ion alone. An additional redox reaction occurred above 4.2 V with a sloped voltage profile as Ti gradually replaced the Ir metal ion. The Ti substitution modulated the overall redox contribution, where the dQ/dV^{-1} curves showed a decrease in the Ir redox contribution while the oxygen redox reaction became more prominent and lengthened above 4.2 V with increasing Ti^{4+} content. As a result, the electrochemical properties changed, with the specific capacity increasing from ≈ 140 to $\approx 175 \text{ mA g}^{-1}$ when $\text{Ti} = 25\%/50\%$, and the capacity dropping to 105 mAh g^{-1} at $\text{Ti} = 75\%$. This result indicates that Ti^{4+} substitution further enables the supplemental redox reaction but reduces the metal redox capability. Thus, it is important to determine the optimal stoichiometry that enables both metal and high-voltage redox capability. The cycling shows the LITO25 and LITO50 to be the most favorable over LIO and LITO75, where especially LITO75 delivers a low discharge capacity ($\approx 105 \text{ mAh g}^{-1}$) and shows the significant voltage drop from the first cycle. As for LITO25 and LITO50, even though similar cycling capability showed up to 5th cycle, LITO50 exhibits a voltage drop and the significant irreversible capacity loss during the first cycle. Thus, the LITO25 composition was selected as the optimal concentration in conducting experiments.^{17,15}

Figure 2a presents the voltage profile for the 1st cycle of LIO and LITO25 at a current rate of 10 mA g^{-1} ($\approx C/21$). The initial charge and discharge capacities were $\approx 170/\approx 140 \text{ mA g}^{-1}$ for LIO and $\approx 202/173 \text{ mA g}^{-1}$ for LITO25, indicating that LITO25 delivered $\approx 30 \text{ mA g}^{-1}$ extra capacity when discharged compared with LIO. This result indicates that oxygen oxidation played a role in the high capacity beyond the Ir metal redox capability. The voltage profile of LITO25 contained four plateaus upon the 1st charging, with average potentials of 3.56, 4.10, 4.35, and 4.47 V, as shown in the inset of Figure 2a. A previous report on conventional LIO revealed two distinct plateaus at potentials of 3.56 and 4.10 V, with the peak at 3.56 V assigned to the Ir redox $4+ \rightarrow 5+$ and the second peak contributing to the Ir redox $5+ \rightarrow 5.5+$, with the phase transition from the initial O3 to the O1 phase with the T3 phase as an intermediate upon the 1st cycling.¹⁷ Notably, the second plateau of LITO25 at $\approx 4.10 \text{ V}$ shows a potential shift toward lower voltage, indicating that the tuned $\text{Ir}^{4+/5+}$ redox potential may have originated from the integrated Ti^{4+} around the Ir^{4+} ions. In addition, the facile redox process of

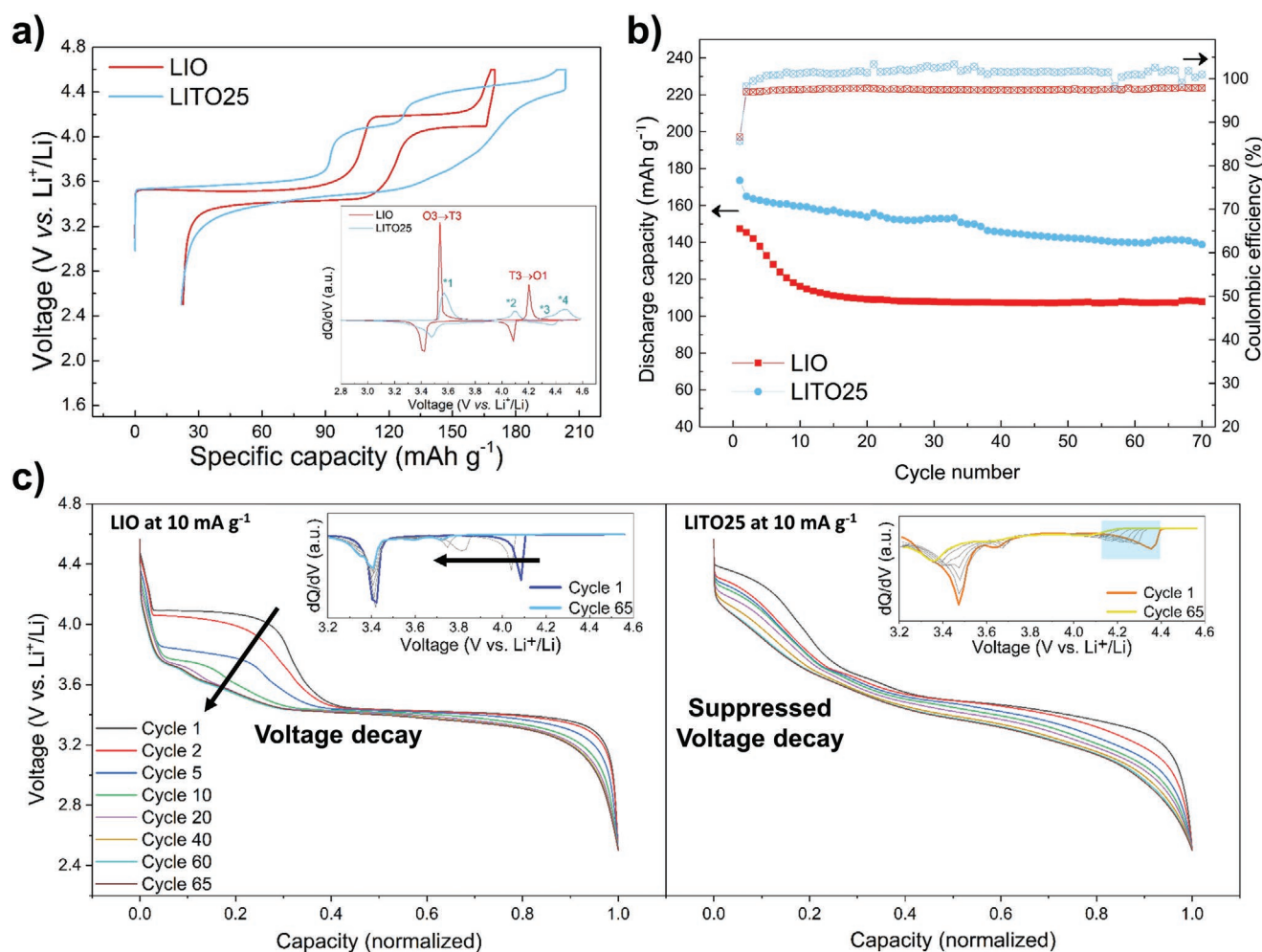


Figure 2. a) Galvanostatic charge/discharge profiles of LIO and LITO25 at a current rate of 10 mA g^{-1} ($C/21$) in the voltage window of 2.5–4.6 V versus Li^+/Li . The inset presents 1st cycle $dQ \text{ dV}^{-1}$ plots of LIO and LITO25. b) Capacity retention and coulombic efficiency of LIO and LITO25 during electrochemical cycling up to 65 cycles. c) Normalized discharge capacities of LIO and LITO25. The inset presents $dQ \text{ dV}^{-1}$ plots of LIO and LITO25 at each cycle.

LITO25 compared with that of LIO was confirmed by the GITT profile in Figure S8, Supporting Information. Further analysis is rationalized and discussed in later sections. The broad asymmetric plateaus with large voltage hysteresis observed at high voltages above $>4.2 \text{ V}$ can be denoted as oxygen redox. This is in line with the previous report on $\text{Li}_2\text{Ir}_{0.75}\text{Sn}_{0.25}\text{O}_3$ (LISO25) and $\text{Li}_2\text{Ru}_x\text{M}_{1-x}\text{O}_3$ ($\text{M} = \text{Ti}, \text{Sn}$) systems, where the oxygen oxidation peaks were typically assigned in the range of 4.2–4.4 V.^[7] The sequential lithiation steps of oxygen un-dimerization and the reduction of $\text{Ir}^{5.5+}$ to Ir^{4+} can be observed in the discharge profile.

Cycling tests were performed on LIO and LITO25 between 2.5 and 4.6 V versus Li^+/Li at a current rate of 10 mA g^{-1} ($C/21$), as shown in Figure 2b. LIO showed abrupt capacity fading up to the 10th cycle, and then, the capacity became steady. In contrast, LITO25 showed gradual fading for 65 cycles, delivering overall enhanced capacity retention and cycling stability with 81% capacity retention for LITO25, compared with 72% for LIO. The cycling stability of LITO25 was preserved even when long-cycling tests were performed at different rates of 5 mA g^{-1}

($C/42$) and 1758 mA g^{-1} ($C/12$) (Figure S9, Supporting Information). The rate capabilities of LIO and LITO25 under different current densities can be assessed in Figure S10, Supporting Information. LITO25 exhibited an enhanced rate capability at all current densities, where $\approx 17\%$ better energy retention was observed up to 1 C, indicating the facile Li de/lithiation chemistry of the LITO25 cathode.

Figure 2c presents the normalized discharge profiles for both LIO and LITO25 until the 65th cycle with $dQ \text{ dV}^{-1}$ profiles as inset figures; the full charge–discharge profiles are presented in Figure S11, Supporting Information. The discharge profiles of LITO25 reveal a smaller voltage decay of $\approx 274 \text{ mV}$ after the 65th cycle compared with that of LIO ($\approx 376 \text{ mV}$). This result is further elaborated with the $dQ \text{ dV}^{-1}$ profiles, with highly symmetric electrochemistry profiles and suppression of the voltage decay observed in the high-voltage region. The stability of LITO25 becomes more evident upon comparison of the results with those in previous studies, with doping of Sn^{4+} in the LIO system resulting in the voltage profile becoming sloped and immediately converting to a S-curve after the 1st cycle

with ≈ 250 meV voltage decay after the 50th cycle for both LIO and LISO25.^[6] In addition, Ti^{4+} integration in $\text{Li}_2\text{Ru}_{0.75}\text{M}_{0.25}\text{O}_3$ ($\text{M} = \text{Ti}, \text{Sn}$) resulted in enhanced electrochemical performance with $\approx 20\%$ capacity retention and improved structural stability compared with that of the Sn^{4+} -doped system.^[13] This finding suggests that the Ti^{4+} -embedded system is able to comparatively retain its redox path even with the activated anionic redox.

The enhanced capacity retention and suppressed voltage decay of LITO25 can be attributed to the robustness of LITO25, with previous studies reporting that Ti^{4+} modification improves the structural stability because of the stronger Ti–O bond energy relative to that of Ir–O together with Ti acting as a supporting structure in the LiM_2 layer, as suggested by the neutron analysis in the previous section. This can be reasoned from the metal–oxygen bonding nature, with a higher electronegativity difference resulting in a stronger bond. The electronegativity difference of the Ti–O bond (1.9) is greater than that of the Ir–O bond (1.48). What's more, previous reports

have shown that migrated metal ions acts as a support in preserving overall cathode framework during (de)lithination process, thereby enhancing the electrochemical performance.^[13,16] The neutron and XRD Rietveld analysis denote Ti^{4+} migration to Li 4 h site with $\approx 1\%$ occupancy, demonstrating the capability of Ti^{4+} ion in retaining the overall stability during electrochemical cycling.

2.3. Crystal Structure Changes Upon Charge/Discharge

To probe the structural changes upon charge/discharge and understand the Li de/intercalation mechanism, in situ XRD analysis was performed at a current rate of 14.06 mAh g^{-1} ($\text{C}/15$) in the voltage range of 2.5–4.6 V versus Li^+/Li . **Figure 3a** presents the XRD patterns of LITO25 during the initial charge/discharge, which demonstrates that the electrochemical reaction occurs via a two-phase reaction of the O3 and O1' phases. Upon charging

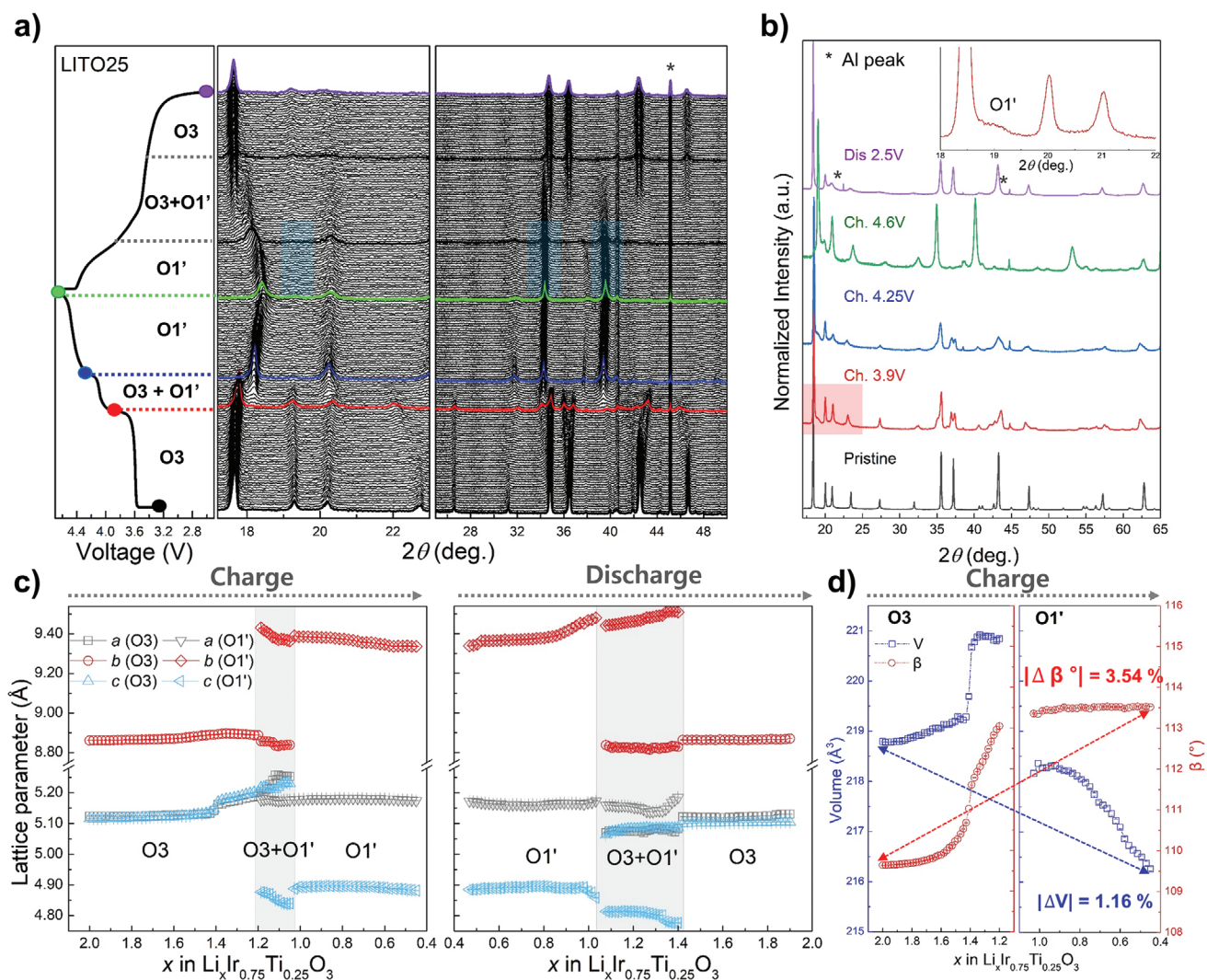


Figure 3. a) In situ XRD patterns for LITO25 cell cycled at a rate of 14.06 mAh g^{-1} ($\text{C}/15$). b) Ex situ XRD patterns of LITO25 electrodes (pristine, charged states of 3.9, 4.25, and 4.6 V, and discharged state of 2.5 V). c) Lattice parameter changes upon charge/discharge of LITO25 electrode obtained from profile fitting of in situ XRD patterns. d) Unit-cell-volume and beta-angle changes during charge process of LITO25.

to 4.02 V, the overall O3 structure was well maintained with broadening of both the main and superstructure XRD peaks, indicating the active Li–M layer mixing as well as the slight loss of crystallinity in the honeycomb layer compared to the pristine state. The new O1' peak started to evolve with the simultaneous disappearance of the O3 phase until 4.21 V; then, the phase transformation to O1' occurred with continuous peak shifts up to 4.6 V, as observed in the ex situ XRD patterns (Figure 3b). Note that the complete disappearance of superstructure peaks in the 2θ range of 20–23° was not observed in the XRD pattern of the LITO25 electrode when charged to 4.6 V, with new peaks appearing at higher angles of 34.9° and 40.2°, which can be indexed to (130) and (220) of the O1 phase, respectively, as shown in Figure 3b. The newly formed peaks correspond to the O1' phase, similar to the O1 phase from LIO, where LIO undergoes the phase transition from the O3 to T3 and O1 phases when charged to 4.6 V, as shown in Figure S12a, Supporting Information. Likewise, the existence of both O3 superstructure peaks as well as the O1' main peak hints that the phase did not completely convert to the O1 phase, indicating that the overall cathode frameworks are well preserved during electrochemical cycling.^[17] On discharge, the phase transitions shifted back continuously to the original O3 phase; however, the superstructure peaks did not fully recover to those of the original state.

The lattice parameter and unit-cell-volume changes are shown in Figure 3c,d. Continuous increases in the lattice parameters and cell volume of the O3 phase were observed during the initial charge process up to 4.02 V (≈ 0.7 Li), with sudden increases of the *a* and *c*-lattice parameters at the subsequent voltage before the new O1' phase appears. The phase separation from O3 to O3 and O1' occurred at ≈ 4.12 V, which may have resulted from the large anisotropic lattice expansion and contraction upon delithiation involving the oxygen redox reaction. The lattice parameters and cell volume of the O1' phase showed a continuous decrease upon further charging to 4.6 V, and on discharge, the lattice parameters returned to the initial values of the O3 phase, denoting the reversible charge/discharge process.

Comparison of the in situ XRD data for LITO25 and LIO led to several intriguing findings. First, Ti⁴⁺ substitution expanded the single-phase reaction region in the O3 phase and overall minimized the phase transition. It is apparent that the O3 phase in LITO25 prolonged the single-phase reaction until 4.02 V compared with that of LIO (3.52 V) with altered phase transitions from O3 to O1', while LIO evolved through multiple-phase transition (O3→T3→O1) during the de-lithiation process when charged to 4.6 V, as described in Figure S12a, Supporting Information. Second, smaller lattice parameter and cell volume changes were confirmed from LITO25 compared with those from LIO. In LIO, de/lithiation resulted in structural change from the initial O3 to the final O1 phase, leading to severe lattice distortion with 8.64% volume decrease and 17.72% $\Delta\beta^\circ$ angle shrinkage (Figure S12b,c, Supporting Information). In contrast, LITO25 exhibited minimized structural distortion, with 1.16% volume decrease and 3.54% $\Delta\beta^\circ$ angle increase, demonstrating that Ti⁴⁺ substitution minimizes phase transitions and ensures structural stability (Figure 3d), which can be correlated to the battery cycling test shown in Figure 2b.

2.4. Valence States of Ir, Ti, and O Ions Upon Charge/Discharge

XAS analyses were performed to probe the redox contributions of Ir and Ti metals during electrochemical cycling and to accurately distinguish between the metal and oxygen redox sections. The spectra were measured at the Ir L₃-edge and Ti K-edge during the 1st cycle of LITO25, with the samples prepared by the ex situ method. Figure 4a presents the Ir L₃-edge X-ray absorption near edge structure (XANES) spectra. The white line (WL) shifted toward higher binding energy by positive ≈ 1.2 eV when charged to 4.4 V, corresponding to an increase in the Ir oxidation state from Ir⁴⁺ to Ir^{5.5+} metal oxidation. The slight WL shifts to lower binding energy by ≈ 0.1 when charged to 4.6 V can be seen as Ir partially oxidized to Ir⁶⁺, as suggested in previous literature.^[7] This finding suggests the limited Ir redox capability beyond the 5.5+ state, implying the involvement of the oxygen redox reaction beyond 4.4 V. On discharge, oxidation resulted in the original Ir⁴⁺ state after discharge to 2.5 V, revealing the linear correlation between Ir oxidation and the WL shift, as shown in the inset figure of Figure 4a. Previous studies on LIO/LISO25 have shown the Ir WL energy difference between Ir⁴⁺ to Ir⁶⁺ to be 1.4 and 2.0 eV,^[7] making it ≈ 0.7 eV per electron loss of Ir metal.^[18] A similar phenomenon was observed for the Li₂Ru_{0.75}Sn_{0.25}O₃ system with 0.7 eV binding energy shift was noted through X-ray photoelectron spectroscopy, further showing the Ru oxidation state changed from Ru⁴⁺ and Ru⁵⁺ corroborating the oxygen oxidation reaction involvement other than conventional metal oxidation.^[14]

Figure 4b presents the Ti K-edge XANES spectra at different charged states. The intensity of the pre-edge peak at $\approx 4,970$ eV increased during charge, implying the distortion of the TiO₆ octahedral structure. The intensity of the discharged spectra was not fully restored to the original intensity, possibly due to the Ti⁴⁺ metal migration from octahedral to tetrahedral sites in the Li layer during the 1st charging followed by the Ti⁴⁺ permanently remaining in the tetrahedral sites, as suggested in a previous study.^[12] The shape change of the XANES spectra at $\approx 4,990$ eV is mainly due to lattice changes, as Ti⁴⁺ has 3d⁰, which cannot go through oxidation. Thus, we conclude that Ti⁴⁺ remains unoxidized and rather acts merely as an anchor in LM₂, as reported in previous studies.^[9a,13]

Extended X-ray absorption fine structure (EXAFS) analysis was consequently performed to further probe the structural modifications on TM–O, as shown in Figures 4c,d. The first shell accounts for metal–oxygen bond lengths of the TMO₆ (TM = Ir or Ti) octahedron, whereas the 2nd shell and beyond account for TM–TM bond lengths, which correspond to an asymmetric honeycomb arrangement involving two or more neighboring TM distances. The EXAFS spectra were not phase-corrected, and the actual distances are ≈ 0.3 – 0.5 Å longer. The results indicate that both the Ir–O and Ti–O bond lengths decrease during charging. This is in line with the in situ XRD data, which indicated gradual volume contraction, as shown in Figure 3e. When fully discharged, the reversible Ir–O is shown, whereas the Ti–O coordination of Ti–O is not fully restored by 0.12 Å, implying the irreversible local structure and lattice distortion. A similar trend was observed in the in situ XRD data, where superstructure peaks did not fully recover upon cell discharge. This result indicates that in-plane cation

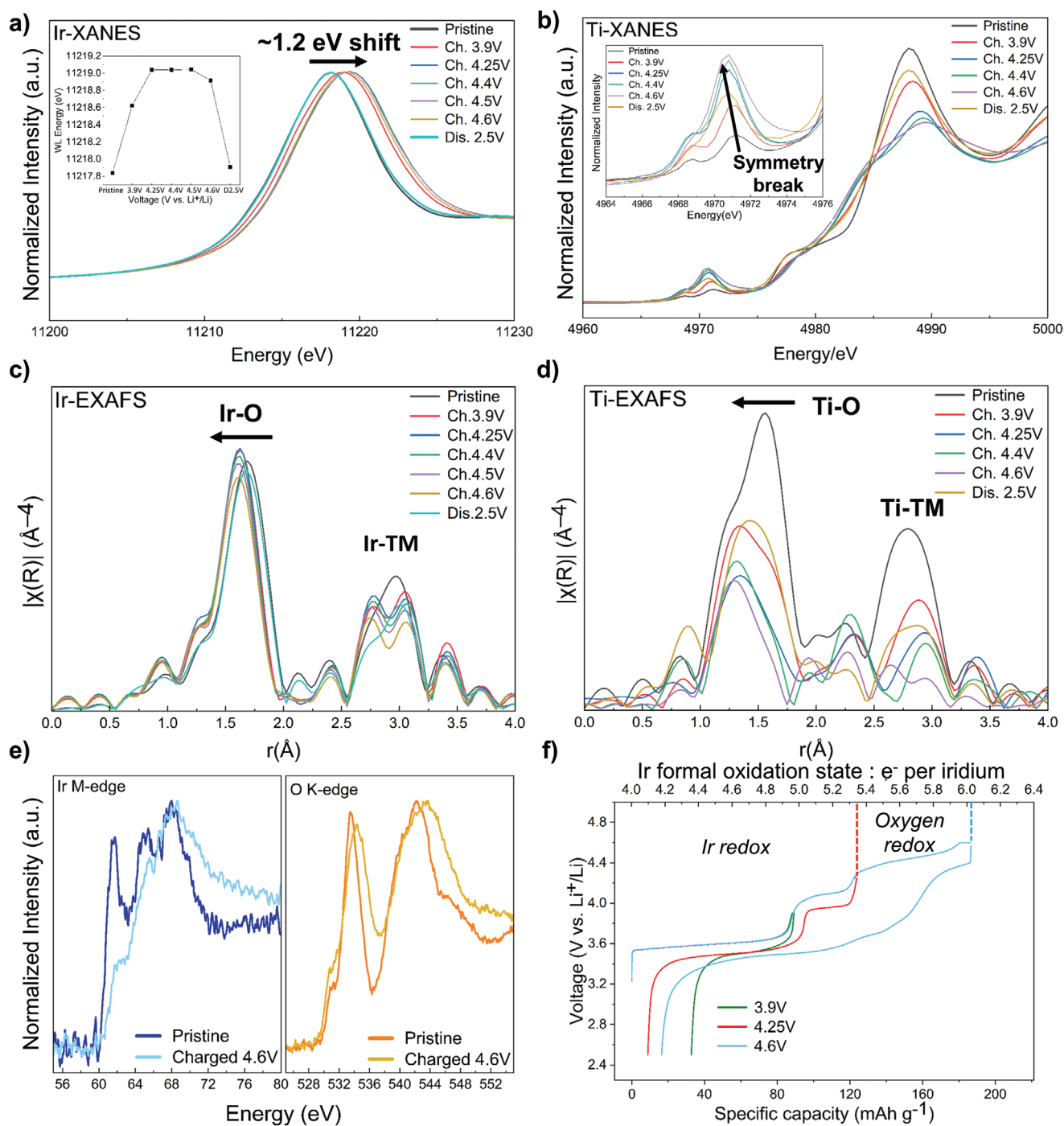


Figure 4. Transmission Ir L₃-edge a) XANES and c) EXAFS spectra measured at selected intermediate states of LITO25 charged at 3.9, 4.25, 4.4, 4.5, and 4.6 V and discharged at 2.5 V. Ti K-edge b) XANES and d) EXAFS spectra of LITO25 charged at 3.9, 4.25, 4.4, and 4.6 V and discharged at 2.5 V. e) TEM EELS spectra of Ir M-edge and O K-edge of LITO25, pristine and charged state of 4.6 V. f) Electrochemical profiles of LITO25 at the first cycle with voltage cutoffs of 3.9, 4.25, and 4.6 V.

ordering has been affected after oxygen redox reaction or Ti⁴⁺ cation rearrangement to Li sites, with the migrated metal stabilizing the overall framework, resulting in improved cyclability and electrochemistry.

Figure 4e presents the electron energy loss spectroscopy (EELS) spectra on the Ir M-edge and O K-edge when the pris-

tine state was compared with that of the fully charged state (4.6 V). The charged Ir M-edge shows a completely new peak shape, with the peak at 61.7 eV completely diminished and its width broadened, reflecting the severe structural change of the Ir–O environment due to the oxidative process. In contrast, the O K-edge showed a decrease in intensity with peak shifts

(≈ 0.9 eV) toward higher energy for both oxygen peaks (at 533.4 and 542.1 eV of the pristine state) while preserving the overall peak shapes, which indicates oxygen oxidation. The participation of oxygen in redox reaction was further confirmed by soft XAS analysis as shown in Figure S13, Supporting Information. These results provide a good understanding of the redox process along the electrochemical curve at different cut-off voltages of LITO25, where the hysteresis started to appear at >4.2 V, indicating the irreversible evolution of the structural changes due to the activated oxygen oxidation, as illustrated in Figure 4f. The stability of Ir and oxygen redox reactions in LITO25 upon electrochemical cycling was further confirmed by Ir L_{3} -edge XANES analysis as shown in Figure S14, Supporting Information, suggesting that repeated cycling does not significantly affect the Ir redox processes in LITO25, while LIO undergoes Ir metal reduction upon cycling.

2.5. Theoretical Evaluation of Oxygen Redox Activity by DFT Calculations

The redox reaction mechanism of LITO25 was further investigated through DFT calculations. The density of state (DOS) calculation was used to understand the redox activity at different

delithiated states ($\text{Li}_2\text{Ir}_{0.75}\text{Ti}_{0.25}\text{O}_3$ and $\text{Li}_{0.5}\text{Ir}_{0.75}\text{Ti}_{0.25}\text{O}_3$), which correspond to respective phases as shown in Figure 5a,b. The results revealed that Ir governs the redox activity in the pristine $\text{Li}_2\text{Ir}_{0.75}\text{Ti}_{0.25}\text{O}_3$ state. Upon charging, the DOS O 2p level was enhanced, indicating that oxygen oxidation accounted for the increased capacity at delithiated states. In addition, the band gap energy decreased as the delithiation occurred, making the oxygen redox more accessible for the redox activity, as discussed in previous studies.^[7,11a,13]

The crystal structures from the DFT results were examined to offer a rationalization of the oxygen redox. It has thus far been suggested that the presence of O–O dimers is a strong indicator of oxygen redox, where the localized two neighboring oxygen dimers are paired to form $\text{O}_2^{(n)-}$ from O^{2-} at the shared edge of neighboring IrO_6 octahedra.^[6,11c,19] The crystal structure exhibits the O–O shortening from 2.91 to 2.46 Å as the material undergoes a charging process from $\text{Li}_2\text{Ir}_{0.75}\text{Ti}_{0.25}\text{O}_3$ to $\text{Li}_{0.5}\text{Ir}_{0.75}\text{Ti}_{0.25}\text{O}_3$, as shown in Figure 5c. It is also worth mentioning that the bond lengths vary nonlinearly between Ir–O and Li–O upon phase transition from the O3 to O1' phase, with the long Ir–O distance shortening from 2.033 to 1.891 Å and the Ti–O distance shortening from 1.998 to 1.930 Å. However, the longest bond length change for Li–O was 2.074 to 2.282 Å. The shortening of TM–O correlates with the in situ

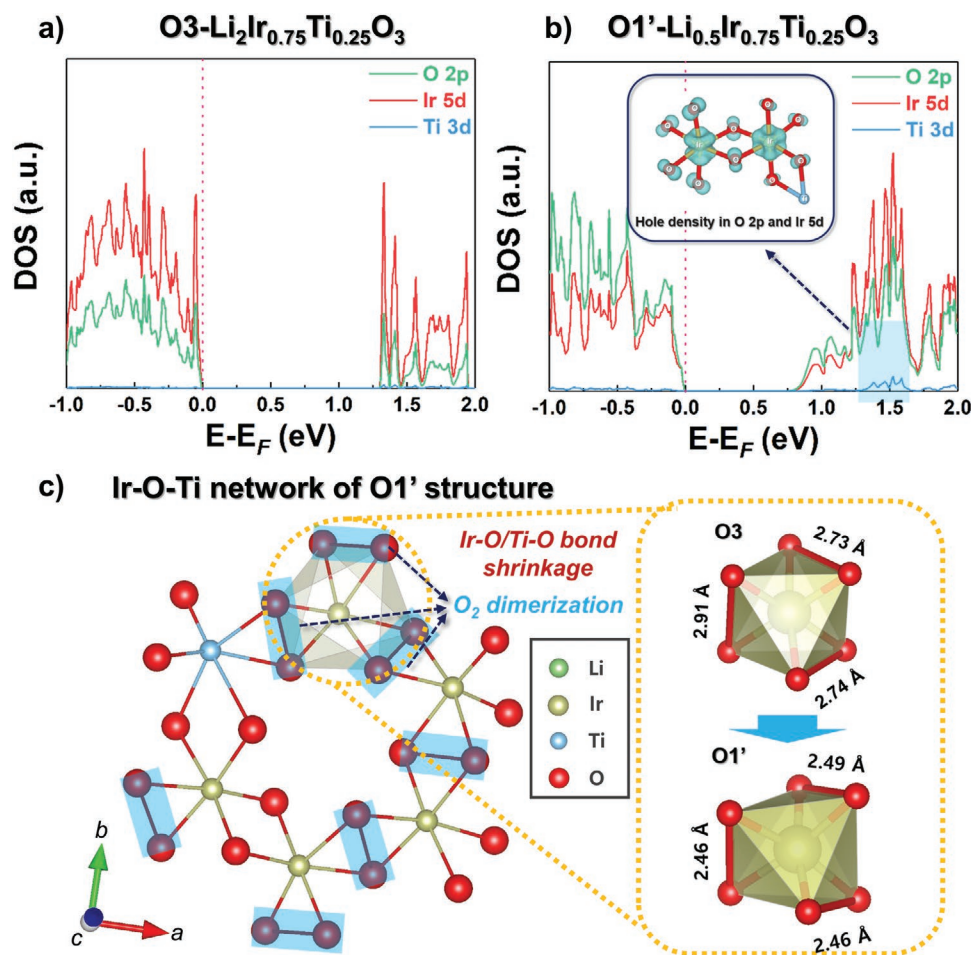


Figure 5. DOS calculation of LITO25 for a) O3 and b) O1' phases. c) DFT representation of O1' phase, showing the overall Ir–O–Ti network structure, and corresponding IrO_6 octahedra forming O_2 dimerization for the respective phases.

XRD and XANES data, where overall contraction of the lattice parameters and TM–O bonds were observed, as also suggested by DFT results, which showed a shorter interlayer distance during phase transitions to O1' (Figure S15, Supporting Information). The Ti–O bond forms a strong ionic bonding nature with surrounding O²⁻ anions, affecting the oxygen octahedral bonding to become uneven, making LITO25 more accessible to O₂ dimerization, as suggested in previous studies.^[19,20] Furthermore, the lengthened Li–O implies the facile de/lithiation during electrochemical reaction, where previous studies have revealed electrons more localized around O ions in Ti–O bonding compared with in Mn–O or Co–O or Ru–O bonds,^[11a,13,21] enabling the improved electronic/ionic conductivity and facilitating lithium-ion transport.

We further attempted to probe the oxygen oxidation mechanism using DFT, employing the out-of-plane antisite defect (Sn_{Li}) and vacancy (V_M) formation model as suggested by Hong et al., where the metal in the LiM₂ layer migrates to 4 h sites in the Li layer, supposed to be enabling the O–O dimer formation across the interlayer between the LiM₂ and Li layers with 1.8-Å bond distance.^[7] Unlike for Sn⁴⁺, the DFT simulation showed that the O–O dimerization was not feasible in the Ti⁴⁺ substituted structure with Ti⁴⁺ at the 4 h site (out-of-plane). Instead, the oxygen oxidation was triggered through the O–O dimerization via the in-plane octahedra within the honeycomb layer. This suggests that the oxygen redox is activated via a different mechanism in LITO25 system and that the local structural effect plays a strong role in triggering different oxygen redox reactions. It was discussed above that large size and low electronegativity of Sn⁴⁺ metal ion in LISO25 induces structural disordering via in plane as well as antisite defect (Sn_{Li}), enabling the facile O–O dimer formation across the interlayers. On contrary, in LITO25, we expect that the strong ionic Ti–O bonding plays an important role in both enhancing the structural stability and inducing the in-plane O–O dimerization in neighboring IrO₆ octahedra as shown in Figure 5c. Due to the small ionic size and high electronegativity of Ti⁴⁺ ion, it allows the stabilized intermediate phases with conserved honeycomb layer through strong bonding and suppressed degradation, making it oxygen redox reaction by in-plane O–O dimer more realizable rather than that by out of plane. This ensures the reversibility of the oxygen redox reaction with improved electrochemical performance.

We believe that unveiling the local environment evolution with the Li (de)intercalation behavior in the high-voltage region is the key to developing advanced battery materials with increased extra capacity and stabilized anionic redox, suggesting that inducing the in-plane and out-of-plane structure via stacking faults could potentially be used to control the degree of oxygen redox response, resulting in enhanced electrochemical properties.

3. Conclusion

A new LITO25 cathode material was successfully synthesized from the conventional LIO layered structure, with the effects of Ti⁴⁺ doping on LIO systems investigated. The newly synthesized LITO25 cathode exhibited improved electrochemical

properties and structural stability, thus stabilizing the oxygen redox plateau in the high-potential region, resulting in suppression of the voltage decay. Combined experimental and computational analyses revealed that Ti⁴⁺ substitution reduces the structural disordering during the de/lithiation, strongly putting the structure together. The prolonged single-phase region with minimized phase transitions in LITO25 further supports this enhanced structural stability. This finding enables us to see the nature of Li-rich materials and offers further physical insights on the local structural effect in triggering the anion redox reaction of O²⁻/O₂⁽ⁿ⁾⁻ as well as the contribution of Ti⁴⁺ to the structural stability, both qualitatively and quantitatively. We believe that this study will provide a fundamental understanding of the anion redox reaction mechanisms and pave a way to designing new promising high-capacity cathode materials.

4. Experimental Section

Synthesis of Li₂Ir_{1-x}Ti_xO₃ (x = 0, 0.25, 0.5, 0.75): Li₂Ir_{1-x}Ti_xO₃ (x = 0, 0.25, 0.5, 0.75) samples were prepared via solid-state synthesis. Stoichiometric amounts of Li₂CO₃ (≥99.0% ACS reagent, Sigma Aldrich), IrO₂ (99.9% metal basis, Korea R&D), and TiO₂ (99.8% trace metals basis, Sigma Aldrich) were mixed by hand grinding. The ground mixture was pelletized under a pressure of 250 kg cm⁻² and heated at 1050 °C for 12 h twice in a box furnace with intermittent grinding.

Structure Characterization: The synthesized Li₂Ir_{1-x}Ti_xO₃ (x = 0, 0.25, 0.5, 0.75) samples were characterized by neutron and XRD analyses. Powder XRD of Li₂Ir_{1-x}Ti_xO₃ (x = 0, 0.25, 0.5, 0.75) and ex situ data were obtained using an Empyrean XRD (Malvern PANalytical, Almelo, Netherlands) equipped with Cu Kα radiation (λ = 1.540598 Å). The measurement was conducted in the 2θ range of 10–80° with a step size of 0.013 and step time of 1 s. In situ charge/discharge XRD data of LITO25 were collected in the 2θ range of 10–80° with a step size of 0.026 and step time of 0.3 s. ND data on Li₂Ir_{1-x}Ti_xO₃ (x = 0, 0.25, 0.5) were obtained using the Echidna high-resolution powder diffractometer at the OPAL research reactor of the Australian Nuclear Science and Technology Organization (ANSTO). The data were collected over the 2θ range of 4–163.95° with step size of 0.05° using a constant wavelength of 1.6215 Å. The particle morphologies and crystal structure were characterized using field-emission TEM (FE-TEM; JEM 2100F, JEOL) at the Korea Basic Science Institute (KBSI).

The valence states of Ir and Ti were analyzed using XAS at beamline 10C (Wide XAFS) and 8C (Nano XAFS) at the Pohang Acceleratory Laboratory (PAL). XAS spectra around the Ir L₃-edge and Ti K-edge were collected in transmission mode with an electron energy of 3 GeV and a current of 400 mA. XAS spectra around the O K-edge were obtained in the total electron yield (transmission yield) method at beamline 6A in PAL.

Electrochemical Analysis: Li₂Ir_{1-x}Ti_xO₃ (x = 0, 0.25) powder samples were mixed with Super-P carbon and polyvinylidene fluoride binder in a mass ratio of 8:1:1 in N-methyl-2-pyrrolidone (99.5%, Sigma Aldrich). The resulting slurry was coated onto aluminum foil, vacuum dried, and roll pressed. Coin-type half cells (CR2032, Wellcos) were assembled using the electrode, a lithium metal counter electrode, a glass microfiber filter (grade GF/F, Whatman) as a separator, and 1 M LiPF₆ in ethylene carbonate/dimethyl carbonate (EC/DMC, 1:1 v/v, PanaXETec) as the electrolyte. All the preparation was performed in an argon-filled glovebox. The cells were cycled in the voltage range of 2.5–4.6 V versus Li⁺/Li at different current densities (5, 10, and 17.58 mA g⁻¹) at 25 °C (WBCS 3000; WonA Tech, Republic of Korea). Ex situ electrode samples were prepared by electrochemical cycling using the coin cells. The cycled coin cells were disassembled, and the electrode samples were rinsed with DMC and dried at 70 °C in a vacuum oven.

Computational Details: DFT calculations were carried out and the projector augmented wave method was implemented in the Vienna ab initio simulation package (VASP).^[22] PAW pseudopotentials^[23] was applied with a plane-wave basis set as implemented in VASP. Perdew–Burke–Ernzerhof parameterization of the generalized gradient approximation (GGA)^[24] was used for the exchange–correlation functional. The Ueff values of Ir and Ti for GGA+U based DFT calculation is 2.75 and 1.5 eV, respectively.^[25] All DFT calculations were based on cut-off energy of 500 eV until the residual forces in the system converged to less than 0.03 eV Å⁻¹ per unit cell. The cluster-assisted statistical mechanics (CASM) software was used for the generation of all Li/vacancy and Ir/Ti configurations for each composition. It was followed by full DFT calculations on a maximum of 40 configurations with the lowest electrostatic energy for each composition, for obtaining the thermodynamically stable crystal structural information.^[26] For the calculations of DOSs, the Heyd–Scuseria–Ernzerhof hybrid functional (HSE06) was used as it has been found to reproduce the O 2p states on transition metal oxides.

Supporting Information

Supporting Information is available from the Wiley Online Library or from the author.

Acknowledgements

M.C. and S.H.S. contributed equally to this work. This research was supported by the National Research Foundation of Korea (NRF) funded by the Ministry of Science and ICT of Korea (Grant No. NRF-2017M2A2A6A05017652, NRF-2018M2A2B3A05074602, NRF-2021R1A2C1014280, and NRF-2020M3H4A1A03084254). This work was also supported by the internal R&D program at KAERI funded by the Ministry of Science and ICT of Korea (524210-21).

Conflict of Interest

The authors declare no conflict of interest.

Data Availability Statement

Research data are not shared.

Keywords

anionic redox reaction, cathodes, Li-rich batteries

Received: February 9, 2021

Revised: April 18, 2021

Published online: July 1, 2021

- [1] a) M. Armand, J.-M. Tarascon, *Nature* **2008**, 451, 652; b) S. Chu, Y. Cui, N. Liu, *Nat. Mater.* **2017**, 16, 16; c) K. Kang, Y. S. Meng, J. Bréger, C. P. Grey, G. Ceder, *Science* **2006**, 311, 977.
 [2] a) J. N. Reimers, J. Dahn, *J. Electrochem. Soc.* **1992**, 139, 2091; b) A. R. Armstrong, P. G. Bruce, *Nature* **1996**, 381, 499; c) A. Rougier, P. Gravereau, C. Delmas, *J. Electrochem. Soc.* **1996**, 143, 1168; d) B. Kang, G. Ceder, *Nature* **2009**, 458, 190.
 [3] a) M. M. Thackeray, C. S. Johnson, J. T. Vaughan, N. Li, S. A. Hackney, *J. Mater. Chem.* **2005**, 15, 2257; b) T. Ohzuku,

- M. Nagayama, K. Tsuji, K. Ariyoshi, *J. Mater. Chem.* **2011**, 21, 10179; c) F. Zhou, X. Zhao, A. van Bommel, X. Xia, J. R. Dahn, *J. Electrochem. Soc.* **2011**, 158, A187; d) G. Assat, D. Foix, C. Delacourt, A. Iadecola, R. Dedryvère, J.-M. Tarascon, *Nat. Commun.* **2017**, 8, 2219; e) W. E. Gent, K. Lim, Y. Liang, Q. Li, T. Barnes, S.-J. Ahn, K. H. Stone, M. McIntire, J. Hong, J. H. Song, Y. Li, A. Mehta, S. Ermon, T. Tyliczszak, D. Kilcoyne, D. Vine, J.-H. Park, S.-K. Doo, M. F. Toney, W. Yang, D. Prendergast, W. C. Chueh, *Nat. Commun.* **2017**, 8, 2091; f) X. Yu, Y. Lyu, L. Gu, H. Wu, S.-M. Bak, Y. Zhou, K. Amine, S. N. Ehrlich, H. Li, K.-W. Nam, X.-Q. Yang, *Adv. Energy Mater.* **2014**, 4, 1300950; g) S.-H. Yu, T. Yoon, J. Mun, S. Park, Y.-S. Kang, J.-H. Park, S. M. Oh, Y.-E. Sung, *J. Mater. Chem. A* **2013**, 1, 2833; h) C. H. Shen, Q. Wang, F. Fu, L. Huang, Z. Lin, S. Y. Shen, H. Su, X. M. Zheng, B. B. Xu, J. T. Li, S. G. Sun, *ACS Appl. Mater. Interfaces* **2014**, 6, 5516.
 [4] a) L. de Biasi, B. Schwarz, T. Brezesinski, P. Hartmann, J. Janek, H. Ehrenberg, *Adv. Mater.* **2019**, 31, 1900985; b) W.-S. Yoon, M. Balasubramanian, K. Y. Chung, X.-Q. Yang, J. McBreen, C. P. Grey, D. A. Fischer, *J. Am. Chem. Soc.* **2005**, 127, 17479.
 [5] a) S. K. Jung, H. Gwon, J. Hong, K. Y. Park, D. H. Seo, H. Kim, J. Hyun, W. Yang, K. Kang, *Adv. Energy Mater.* **2014**, 4, 1300787; b) W. Hua, S. Wang, M. Knapp, S. J. Leake, A. Senyshyn, C. Richter, M. Yavuz, J. R. Binder, C. P. Grey, H. Ehrenberg, S. Indris, B. Schwarz, *Nat. Commun.* **2019**, 10, 5365; c) J. Yan, X. Liu, B. Li, *RSC Adv.* **2014**, 4, 63268.
 [6] E. McCalla, A. M. Abakumov, M. Saubanère, D. Foix, E. J. Berg, G. Rousse, M.-L. Doublet, D. Gonbeau, P. Novák, G. Van Tendeloo, R. Dominko, J.-M. Tarascon, *Science* **2015**, 350, 1516.
 [7] J. Hong, W. E. Gent, P. Xiao, K. Lim, D.-H. Seo, J. Wu, P. M. Csernica, C. J. Takacs, D. Nordlund, C.-J. Sun, K. H. Stone, D. Passarello, W. Yang, D. Prendergast, G. Ceder, M. F. Toney, W. C. Chueh, *Nat. Mater.* **2019**, 18, 256.
 [8] a) C. Liang, F. Kong, R. C. Longo, C. Zhang, Y. Nie, Y. Zheng, K. Cho, *J. Mater. Chem. A* **2017**, 5, 25303; b) T. Weigel, F. Schipper, E. M. Erickson, F. A. Susai, B. Markovsky, D. Aurbach, *ACS Energy Lett.* **2019**, 4, 508; c) M. Zubair, G. Li, B. Wang, L. Wang, H. Yu, *ACS Appl. Energy Mater.* **2019**, 2, 503; d) D.-H. Seo, J. Lee, A. Urban, R. Malik, S. Y. Kang, G. Ceder, *Nat. Chem.* **2016**, 8, 692.
 [9] a) S. Wang, Y. Li, J. Wu, B. Zheng, M. J. McDonald, Y. Yang, *Phys. Chem. Chem. Phys.* **2015**, 17, 10151; b) Z. Q. Deng, A. Manthiram, *J. Phys. Chem. C* **2011**, 115, 7097; c) Y. Mo, L. Guo, H. Jin, B. Du, B. Cao, Y. Chen, D. Li, Y. Chen, *J. Power Sources* **2020**, 448, 227439.
 [10] a) N. H. Vu, J. C. Im, S. Unithrattil, W. B. Im, *J. Mater. Chem. A* **2018**, 6, 2200; b) S. Wang, J. Yang, X. Wu, Y. Li, Z. Gong, W. Wen, M. Lin, J. Yang, Y. Yang, *J. Power Sources* **2014**, 245, 570.
 [11] a) C. Zhao, Z. Yao, J. Wang, Y. Lu, X. Bai, A. Aspuru-Guzik, L. Chen, Y.-S. Hu, *Chem* **2019**, 5, 2913; b) X. Cao, X. Li, Y. Qiao, M. Jia, F. Qiu, Y. He, P. He, H. Zhou, *ACS Energy Lett.* **2019**, 4, 2409; c) T. Wang, G.-X. Ren, Z. Shadiké, J.-L. Yue, M.-H. Cao, J.-N. Zhang, M.-W. Chen, X.-Q. Yang, S.-M. Bak, P. Northrup, P. Liu, X.-S. Liu, Z.-W. Fu, *Nat. Commun.* **2019**, 10, 4458; d) C. Li, C. Zhao, B. Hu, W. Tong, M. Shen, B. Hu, *Chem. Mater.* **2020**, 32, 1054.
 [12] M. Sathiyá, A. M. Abakumov, D. Foix, G. Rousse, K. Ramesha, M. Saubanère, M. L. Doublet, H. Vezin, C. P. Laisa, A. S. Prakash, D. Gonbeau, G. Van Tendeloo, J. M. Tarascon, *Nat. Mater.* **2015**, 14, 230.
 [13] A. K. Kalathil, P. Arunkumar, D. H. Kim, J.-W. Lee, W. B. Im, *ACS Appl. Mater. Interfaces* **2015**, 7, 7118.
 [14] M. Sathiyá, G. Rousse, K. Ramesha, C. P. Laisa, H. Vezin, M. T. Sougrati, M. L. Doublet, D. Foix, D. Gonbeau, W. Walker, A. S. Prakash, M. Ben Hassine, L. Dupont, J. M. Tarascon, *Nat. Mater.* **2013**, 12, 827.
 [15] M. Sathiyá, K. Ramesha, G. Rousse, D. Foix, D. Gonbeau, A. S. Prakash, M. L. Doublet, K. Hemalatha, J. M. Tarascon, *Chem. Mater.* **2013**, 25, 1121.

- [16] a) H. Zhao, Y. Shi, L. Xue, Y. Cheng, Z. Hu, X. Liu, *J. Energy Chem.* **2019**, *33*, 9; b) B. Mortemard de Boisse, G. Liu, J. Ma, S.-I. Nishimura, S.-C. Chung, H. Kiuchi, Y. Harada, J. Kikkawa, Y. Kobayashi, M. Okubo, A. Yamada, *Nat. Commun.* **2016**, *7*, 11397; c) M. Han, Z. Liu, X. Shen, L. Yang, X. Shen, Q. Zhang, X. Liu, J. Wang, H.-J. Lin, C.-T. Chen, C.-W. Pao, J.-L. Chen, Q. Kong, X. Yu, R. Yu, L. Gu, Z. Hu, X. Wang, Z. Wang, L. Chen, *Adv. Energy Mater.* **2020**, *10*, 2002631; d) S. Liu, Z. Liu, X. Wang, S.-C. Liao, R. Yu, Z. Wang, Z. Hu, C.-T. Chen, X. Yu, X. Yang, L. Chen, *Adv. Energy Mater.* **2019**, *9*, 1901530; e) Q. Xie, W. Li, A. Manthiram, *Chem. Mater.* **2019**, *31*, 938.
- [17] B. Mortemard de Boisse, M. Reynaud, J. Ma, J. Kikkawa, S.-I. Nishimura, M. Casas-Cabanas, C. Delmas, M. Okubo, A. Yamada, *Nat. Commun.* **2019**, *10*, 2185.
- [18] A. J. Perez, Q. Jacquet, D. Batuk, A. Iadecola, M. Saubanère, G. Rousse, D. Larcher, H. Vezin, M.-L. Doublet, J.-M. Tarascon, *Nat. Energy* **2017**, *2*, 954.
- [19] P. E. Pearce, A. J. Perez, G. Rousse, M. Saubanère, D. Batuk, D. Foix, E. McCalla, A. M. Abakumov, G. Van Tendeloo, M.-L. Doublet, J.-M. Tarascon, *Nat. Mater.* **2017**, *16*, 580.
- [20] P. E. Pearce, G. Assat, A. Iadecola, F. Fauth, R. Dedryvère, A. Abakumov, G. Rousse, J.-M. Tarascon, *J. Phys. Chem. C* **2020**, *124*, 2771.
- [21] I. M. Markus, F. Lin, K. C. Kam, M. Asta, M. M. Doeff, *J. Phys. Chem. Lett.* **2014**, *5*, 3649.
- [22] a) G. Kresse, D. Joubert, *Phys. Rev. B* **1999**, *59*, 1758; b) G. Kresse, J. Furthmüller, *Comput. Mater. Sci.* **1996**, *6*, 15; c) G. Kresse, J. Furthmüller, *Phys. Rev. B* **1996**, *54*, 11169.
- [23] P. E. Blöchl, *Phys. Rev. B* **1994**, *50*, 17953.
- [24] J. P. Perdew, K. Burke, M. Ernzerhof, *Phys. Rev. Lett.* **1996**, *77*, 3865.
- [25] a) A. Subedi, *Phys. Rev. B* **2012**, *85*, 020408; b) Y. Wang, J. Liu, B. Lee, R. Qiao, Z. Yang, S. Xu, X. Yu, L. Gu, Y.-S. Hu, W. Yang, K. Kang, H. Li, X.-Q. Yang, L. Chen, X. Huang, *Nat. Commun.* **2015**, *6*, 6401.
- [26] A. Van der Ven, J. C. Thomas, Q. Xu, J. Bhattacharya, *Math. Comput. Simulat.* **2010**, *80*, 1393.